

# Hydrodynamic focusing with a microlithographic manifold: controlling the vertical position of a focused sample

Matthew J. Kennedy · Scott J. Stelick ·  
Sasha L. Perkins · Li Cao · Carl A. Batt

Received: 27 November 2008 / Accepted: 28 January 2009 / Published online: 17 February 2009  
© Springer-Verlag 2009

**Abstract** A microfluidic manifold has been designed, fabricated, and tested that hydrodynamically focuses a sample into the center of a microchannel and provides control over the vertical position of the sample via the flow-rates of the focusing fluids. To characterize the focusing action, a mixing experiment was performed in which the sample fluid and focusing fluid contained different fluorescent dyes. By sweeping the ratio of the rate of the top focusing fluid to the rate of the bottom focusing fluid, the sample was positioned first near the top of the microchannel and then translated downward in steps to the bottom of the microchannel. Images were obtained with confocal microscopy, and the presumptive concentration distributions were computed using multiphysics software. The simulations were shown by direct visual comparison with the experimental images to accurately predict the distributions of fluids in our device. In order to quantitatively compare the two data sets, the images and simulations were analyzed using a simple center-of-mass measurement, and according to this measurement, the simulations accurately predicted the vertical position the focused sample.

## 1 Introduction

Microfluidic manifolds are becoming important for applications in flow cytometry (McClain et al. 2001), gelation of

microfibers (Shin et al. 2007), self-assembly of nanoparticles (Laulicht et al. 2008), and the study of protein folding (Pollack et al. 2001). Focusing in microscale laminar flow devices has been achieved via several mechanisms including dielectrophoresis (Holmes et al. 2006), electroosmosis (Kohlheyer et al. 2008), optical gradient (Zhao et al. 2007), ultrasound (Goddard et al. 2007), and hydrodynamic pressure. Hydrodynamic focusing is the method employed in this study and is achieved by applying a pressure differential across the inputs and output(s) of the manifold.

Vertical steering of a centrally focused fluid stream in a planar microfluidic device is useful for developing portable optical biosensors. Optical biosensors historically have relied on mechanical micropositioning equipment to align the flow-cell with the optical detection system. In the development of microfabricated flow cytometers, several groups have taken steps to eliminate the micropositioning equipment by imbedding integrated optics directly into the flow-cell (Fu et al. 2004; Tung et al. 2004; Wang et al. 2004). In such static arrangements where the optical components remain permanently fixed in their positions, the ability to control the vertical position of the particle stream by adjusting the flow-rates of the focusing fluids provides an attractive method for tuning the alignment between the sample and the optical detection system.

The first microfluidic hydrodynamic focusing devices focused a sample from two sides into a thin columnar stream (Knight et al. 1998). Initial designs for focusing not only from the sides but also from above and below involved several fabrication steps with as many as five-layers of manifold housing (Sundararajan et al. 2004). Recent efforts have focused on fabrication simplicity. Manifolds capable of out-of-plane focusing have been

---

M. J. Kennedy (✉) · L. Cao  
Department of Electrical and Computer Engineering,  
Cornell University, Ithaca, NY, USA  
e-mail: mjk67@cornell.edu

S. J. Stelick · S. L. Perkins · C. A. Batt  
Department of Food Science, Cornell University,  
Ithaca, NY, USA

constructed from two patterned microfluidic layers (Nieuwenhuis et al. 2003; Simonnet and Groisman 2005; Chang et al. 2007); these devices function by overlapping the channels of the first layer with those of the second layer at junctions where the sample is impinged by fluid from the adjoining layer.<sup>1</sup> Using several-stages of focusing, Nieuwenhuis et al. focused a sample from above, below, and from the sides, thereby maneuvering the sample into the geometric center of the microchannel. By adjusting the flow-rates of the various fluid inputs, the focused stream was moved up and down and also to the sides, as demonstrated by finite element simulations and brightfield microscopy. Similar devices consisting of four focusing stages (Simonnet and Groisman 2005) and three focusing stages (Chang et al. 2007) were subsequently studied using single-color confocal microscopy. In these studies, cross-sectional confocal microscopy images were obtained showing the sample focused into a stream small in cross-section compared with the dimensions of the microchannel.

Here, we describe a two-layer manifold following a design similar in concept to Chang et al. 2007 but containing only two-stages of focusing instead of three-stages. This advance reduces the number of fluid inputs required for three-dimensional focusing.

The effect of adjusting the upper and lower focusing flow-rates on the distribution of fluids in our device was investigated by performing a mixing experiment in which the sample fluids contained fluorescein and the focusing fluids contained rhodamine. Images were obtained under a confocal microscope, and concentration distributions were extracted from these images using a series of image processing procedures. For comparison with the experimental images, the presumptive concentration distributions were computed using ANSYS computational fluid dynamics software. To the knowledge of the authors, this is the first study in which a microfluidic focusing manifold has been imaged by two-color confocal microscopy, and this is the first study in which the center-of-mass of the focused stream has been measured relative to the top and bottom walls of the microchannel by analysis of cross-sectional confocal microscopy images. In this paper, we present direct and quantitative comparisons between the images and the simulations, and we demonstrate the capability of this new manifold for controlled out-of-plane steering of the focused sample.

<sup>1</sup> A single-layer planar microfluidic device has also been used to focus a sample into the center of a microchannel (Mao et al. 2007); however, it remains unclear whether this device can be used to control the vertical position of the sample via straightforward adjustment to the relative flow-rates due to its reliance on the transverse transport mechanism popularly known as “microfluidic drifting”.

## 2 Description of the manifold

The manifold was constructed from two complementary pieces of poly-dimethyl siloxane (PDMS). The dimensions of the manifold were  $h = 125 \mu\text{m}$ ,  $w_1 = 125 \mu\text{m}$ ,  $w_2 = 50 \mu\text{m}$ , and  $w_3 = 50 \mu\text{m}$ , as illustrated in Fig. 1a. The sample was applied to the first input at volumetric rate  $U_1$ , and focusing fluid was applied to the focusing inputs at rates  $U_2$  and  $U_3$ , as illustrated in Fig. 1b. The flow-cell contained a total of five fluid inputs. Focusing fluid was applied at each focusing stage by a symmetric pair of fluid inputs from opposite sides of the main microchannel;<sup>2</sup> therefore, the total flow-rate was  $U_0 = U_1 + 2U_2 + 2U_3$ . For the duration of the experiment, the flow-cell was operated under continuous flow conditions at Reynolds number  $Re = 2.72$ , which corresponds to a total volumetric flow-rate of  $U_0 = 20.4 \mu\text{L}/\text{min}$  (2.20 cm/s). The ratio of sample fluid to total fluid was fixed at  $U_1/U_0 = 1/10$ .

## 3 Methods

### 3.1 Fabrication

The flow-cell was fabricated by bonding together two patterned pieces of PDMS using a contact-aligner. Briefly, two polydimethylsiloxane (PDMS) masters were fabricated by patterning polyimide resist onto silicon wafers with photolithography. A thickness of resist of  $125 \mu\text{m}$  was obtained by applying two rounds of spin-coating of SU8-75 (Microchem Corporation, USA) at 2375-RPMs for 40 s for each silicon wafer. Each round of spin-coating was followed by 20 min baking at  $95^\circ\text{C}$  on a hotplate. After cooling, the coated wafer was exposed to ultraviolet light through a patterned chrome mask and then post-exposure baked for 12 min at  $95^\circ\text{C}$ . The wafers were chemically developed to remove resist from all unexposed locations and then rinsed with water followed by Isopropyl Alcohol. After rinsing, PDMS was spun onto the masters at 250-RPMs for 60 s in order to obtain molds of uniform thickness for the subsequent contact alignment procedure. The PDMS was then cured by baking at  $70^\circ\text{C}$  for 45 min.

The critical step in the fabrication of this flow-cell was the alignment of the two pieces of PDMS relative to one another as they were brought into contact. Immediately preceding alignment, the two pieces were peeled from their masters and exposed to a 200-W oxygen plasma (Glen Technologies 1000p), patterned side up, for 20 s. Next, the

<sup>2</sup> If desired, the total number of flow-cell inputs could be reduced from five to three by connecting, on-chip, the focusing inputs for each focusing stage (see Chang et al. 2007). In this case, the total flow-rate would be  $U_0 = U_1 + U_2 + U_3$ .

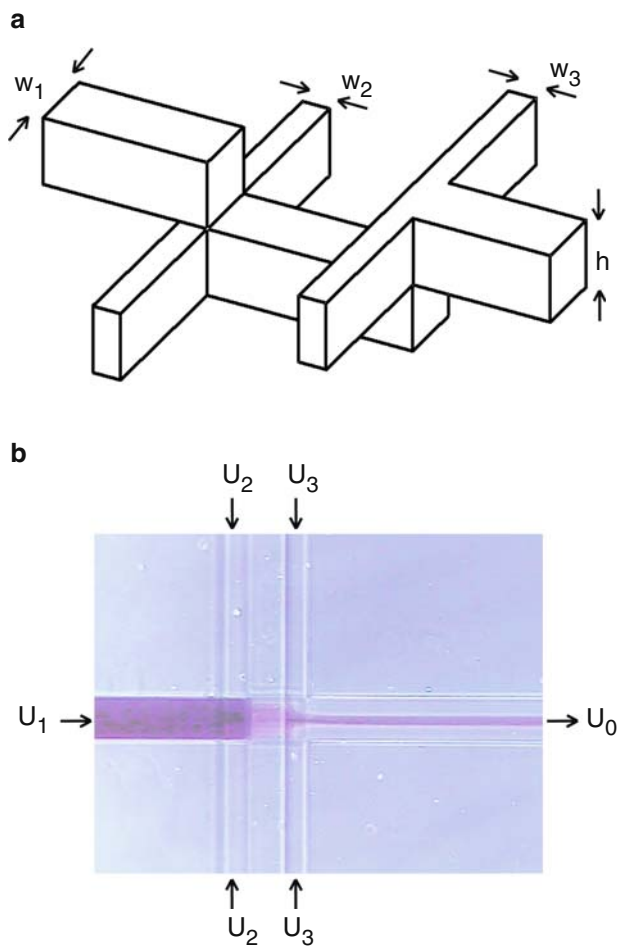


**Fig. 1** Schematic and optical micrograph of the manifold. **a** Schematic of the geometry and dimensions of the manifold. The height of all features is  $h$ . The width of the microchannel guiding the fluid under focusing is  $w_1$ . The widths of the microchannels guiding the focusing fluids are  $w_2$  and  $w_3$ . **b** Optical micrograph showing the flow-cell under continuous-flow operation with food coloring added to the fluid under focusing. The fluid under focusing was applied at volumetric rate  $U_1$  ( $\mu\text{L}/\text{min}$ ); the focusing fluid was applied at rates  $U_2$  and  $U_3$  at the first and second focusing junctions

pieces were placed into aligned contact using a contact aligner (III-HR, Hybrid Technology Group, USA) and subsequently baked for 30 min at  $70^\circ\text{C}$  to achieve permanent bonding. The flow-cells were packaged by connecting tubing lines (Tygon Tubing PVC 0.020", Small Parts, Inc.) to the input of each fluid channel via 27-gauge stainless steel tubing (Small Parts, Inc.).

### 3.2 Simulations

Analysis of two-species transport was performed using commercially available finite element-based software. The flow-cell geometry was defined in ANSYS Multiphysics 10.0 as a 3D FLOTRAN-142 element and meshed with an element edge length of  $5\ \mu\text{m}$ . A load of Species 1, molecular

weight 480 g/mol in water, corresponding to fluorescein, was applied to the central input, and a load of Species 2, molecular weight 330 g/mol in water, corresponding to rhodamine, was applied to the focusing inputs. A mass diffusion coefficient of  $5e^{-6}\ \text{cm}^2/\text{s}$  was assumed for both species. A steady-state solution was obtained by solving, together, the Navier–Stokes equation and the convection–diffusion equation using 60 global iterations of the ANSYS preconjugated residual method solver. From this solution, a contour plot was obtained of the concentration distribution of fluorescein over the volume of the manifold. The color-map was defined in ANSYS such that the range of normalized values of concentration,  $[0, 1]$ , mapped linearly to the range of pixel values  $[0, 255]$ . One contour plot was obtained for the concentration of fluorescein, and another contour plot was obtained for the concentration of rhodamine. The two contour plots were exported as TIF files and then, using ImageJ Image Processing Software, were overlaid onto the same image. Cross-sectional images were obtained by altering the viewpoint in ANSYS from three-dimensional view to cross-sectional view and then repeating the export and overlay procedure.

### 3.3 Confocal microscopy

Experimental images of the distributions of fluids were obtained using an inverted laser-scanning spectral confocal microscope (LSM 510-META, Zeiss, Inc.). The microscope is fitted with two excitation sources: a 30-mW Argon Laser (471, 488 nm) and a 15-mW diode-pumped solid-state laser (561 nm). The microscope acquires spectral image data by using a grating to disperse the signal onto a multidetector array. One detector was filtered to detect fluorescence from the fluorescein-labeled fluids in the range of 505–555 nm, and the other detector was filtered to detect fluorescence from the rhodamine-labeled fluids in the range of 575–650 nm. Line-wise multi-tracking was used to further reduce spectral cross-talk by eliminating the simultaneous emission of both chromophores by both excitation sources. Multi-tracking refers to the electronic control of the scanners and laser lines to switch the excitation wavelength between line-scans (Dickinson et al. 2001). Moreover, the 471-nm line of the Argon laser was used for excitation of the fluorescein because the shorter-wavelength mode of excitation reduced the spectral bleedthrough of fluorescence from rhodamine into the green-channel PMT compared to the 488-nm line.

The flow-cell was mounted on the sample holder of the microscope and syringe pumps were placed in proximity (PHD 2000, Harvard Instruments). The sample contained 0.2 mM fluorescein in Tris Buffer pH 8.0, and the sheath fluid contained 0.2 mM Rhodamine 6G in water. Particulates were eliminated from both solutions prior to the

experiment using 0.45- $\mu\text{m}$  syringe filters (21053-25, Corning, USA). The flow-cell was operated under continuous-flow conditions at Reynolds number  $Re = 2.72$  for the duration of the experiment. Between the adjustment to the flow-rates and the acquisition of an experimental image, 5 min time was allowed to pass to ensure that each image represented the steady-state distribution. On a few occasions, instabilities arose when an air bubble entered the microchannel as verified by direct observation through the eyepieces of the microscope. When this occurred, time was allowed until the air bubble had passed, and then an image was recorded after the fluids had returned to their steady-state distribution.

Images were scanned through a cross-section of the microchannel using a 20 $\times$  microscope objective. The distance between the depths of successive scan-lines was 1.0  $\mu\text{m}$ , and the total depth of the  $yz$ -scan was typically 160  $\mu\text{m}$ . The horizontal scan-resolution was 0.29  $\mu\text{m}$ , and the width of the scan was 148  $\mu\text{m}$ . Therefore, a raw  $yz$ -scan typically contained  $512 \times 160$  rectangular pixels. These data were extrapolated by the Zeiss LSM Imaging Software accompanying the microscope to deliver images containing square-pixels, with each pixel representing an area of  $0.29 \mu\text{m} \times 0.29 \mu\text{m}$ . The resulting two-color images typically contained  $512 \times 554$  pixels, and these were exported as TIF files for subsequent processing and analysis.

### 3.4 Image analysis

Images were imported into MATLAB for processing. Each pixel contained values for red, green, and blue, and the pixel blue-values were all zero. Therefore, each image could be thought of as an overlay of one green image and one red image onto the same grid of pixels, where the red image contained intensity values detected by the red-channel PMT,  $I_R(x, y)$ , and the green image contained the intensity values detected by the green-channel PMT  $I_G(x, y)$ . Therefore, each pixel contained red-values  $I_R$  and green-values  $I_G$  each in the range of 0–255.

#### 3.4.1 Image registration

Our image registration procedure fit the walls of the microchannel with a rectangle by first segmenting the image and then fitting the segmented image with horizontal and vertical lines. Segmentation was achieved with the Sobel Operator using the *edge()* function in MATLAB. Next, a horizontal line was fit to the top edge by minimizing the sum of the squares of differences between the pixels of the detected top edge and the horizontal line. The bottom edge and the left and right edges were then obtained in the same manner. The error associated with locating the top and bottom walls of the microchannel was estimated by calculating the standard

deviation of the Sobel-detected pixels about the fitted edge; specifically,  $\sigma = \sqrt{\frac{1}{N} \sum_{i=1}^N (y_i - y_{\text{FIT}})^2}$ . This error did not change noticeably during the sweeping of the focusing flow-rates.

#### 3.4.2 Spectral unmixing

Spectral unmixing was performed in order to remove the contribution of rhodamine fluorescence from the pixel green-values of the images. Briefly, a specific fraction of the pixel red-values was subtracted from the pixel green-values of the images. This fraction was calculated from the flat-field image in which all of the fluids were loaded with rhodamine, as explained in detail in [Appendix](#).

#### 3.4.3 Depth-dependence compensation

Depth-dependence compensation was performed according to a linear mathematical correction method. Briefly, the brightness of the image was observed to decay with depth. The slope of decay of brightness was measured separately for the pixel red-values and green-values by analyzing field images in which the microchannel contained only rhodamine or only fluorescein, respectively. Based on these calculations, the depth-decay was removed from the experimental images using a linear transformation, as explained in detail in [Appendix](#).

### 3.5 Locating the center of mass of the fluorescein

The center of mass of the fluorescein-labeled fluid was calculated according to the usual formula:

$$y_{\text{CM}} = \frac{\sum_{i,j} y_j \cdot I'_G(x_i, y_j)}{\sum_{i,j} I'_G(x_i, y_j)},$$

where  $x_i$  and  $y_j$  refer to pixels measured relative to the best-fit horizontal and vertical walls of the microchannel, and  $I'_G$  refers to the pixel green-values of the image post-processing. This calculation was implemented with our image analysis program, in MATLAB, using a *for* loop. The error associated with measuring the value of the center of mass,  $y_{\text{CM}}$ , was dominated by the error associated with measuring the locations of the bottom and top walls of the microchannel, which was described in Sect. 3.4.

## 4 Results and discussion

### 4.1 Simulation

The concentration distributions of fluorescein and rhodamine were calculated over the volume of the manifold

using ANSYS Multiphysics Computational Fluid Dynamics Software. Our simulations predicted that the sample would become sheathed on all sides in a cylindrical manner as shown in Fig. 2a, where the ratio of the rate of the top focusing fluid to the rate of the bottom focusing fluid was  $U_3/U_2 = 1.5$ . The focusing process takes place in two

steps: at the first junction, the sample is impinged from below by focusing fluids from the bottom layer, and at the second junction, the sample is impinged from above by focusing fluids from the top layer, as shown in Fig. 2b. A vertical slice through the center of the channel along the direction of flow is shown in Fig. 2c.

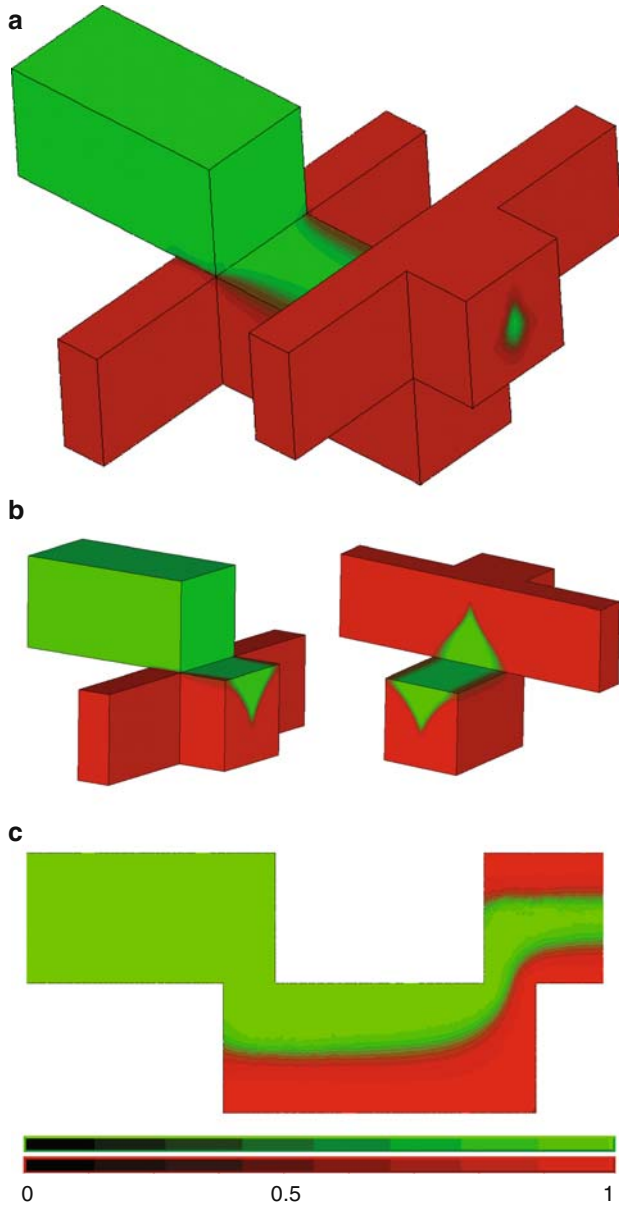


**Fig. 2** ANSYS simulations of two-species mixing. Concentration distributions are shown in which the sample fluid contained fluorescein and the focusing fluid contained rhodamine. **a** Three-dimensional view; **b** three-dimensional view broken into two pieces showing the species distributions between the first and second stages of focusing. **c** Cross-sectional view taken vertically through the center of the main channel along the direction of flow. The flow parameters used for the simulations shown in this figure were Reynolds number  $Re = 2.72$ , focusing ratio  $U_3/U_2 = 1.5$ , and sample-to-total fluid fraction  $U_1/U_0 = 1/10$ . These parameters correspond to individual flow-rates of  $U_1 = 2.04 \mu\text{L}/\text{min}$ ,  $U_2 = 3.67 \mu\text{L}/\text{min}$ , and  $U_3 = 5.51 \mu\text{L}/\text{min}$

#### 4.2 Microscopy

The distributions of fluids at the output of the manifold were imaged by scanning through the depth of the microchannel using a confocal microscope. The focusing ratio,  $U_3/U_2$ , was varied, and several images were obtained. For small values of  $U_3/U_2$ , the sample was positioned near the top of the microchannel as shown in Fig. 3a, whereas for large values of  $U_3/U_2$ , the sample was positioned near the bottom of the microchannel as shown in Fig. 3e. In the case of  $U_3/U_2 = 1.5$ , the sample fluid was sheathed on all sides and was positioned near the geometric center of the microchannel as shown in Fig. 3c.

Similar distributions were observed in the simulations and the experimental images regarding not only the vertical position but also the shape of the focused stream. For

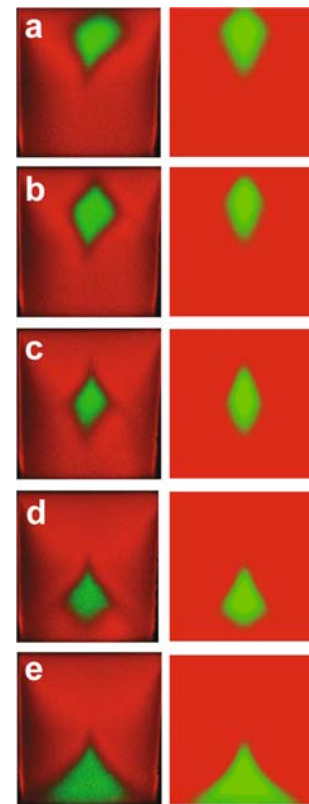


**Fig. 3** Fluorescence micrographs and simulations showing the distribution of the fluids at the output of the manifold. Confocal microscopy images are shown at left and simulations are shown at right for  $U_3/U_2$  equal to **a** 0.012, **b** 0.20, **c** 1.5, **d** 11, and **e** 190

example, when the top and bottom focusing fluids were applied at similar rates, the focused stream took the form of an ellipse with a height of approximately twice its width, as in seen by inspection of Fig. 3c. In contrast, when the top focusing fluids were applied at a rate greater than the bottom focusing fluids, the focused stream took the form of an isosceles triangle with its base lying along the bottom wall of the microchannel, as in Fig. 3e. Notably, the shapes of the distribution of fluids were incongruent for the cases where the sample was positioned near the top versus the bottom of the microchannel (compare Fig. 3a, e). We suggest that this incongruence arose from an absence of reflection symmetry in the geometry of the manifold about the plane dividing the main microchannel into its upper and lower halves, i.e., the plane at  $y = 0.5$ .

### 4.3 Image analysis

Images were processed and then measured to yield the vertical position of the center of mass of the fluorescein-containing fluids. For this purpose, an image analysis program was written in MATLAB so that all images were processed and analyzed using the same sequence of steps. Our program consists of four procedures: (1) image registration, (2) spectral unmixing, (3) depth-dependence compensation, and (4) measurement of the center of mass of the fluorescein-labeled fluids. The first procedure aligns the images to a common origin; the second and third procedures restore the images of two optical effects: spectral bleedthrough and depth-dependence of fluorescence intensity; the fourth procedure provides a quantitative measurement describing the location of the focused sample.

#### 4.3.1 Image registration

An image registration procedure was developed to locate the geometric center of the microchannel in each image. This location provided a reference point to which the various images were subsequently aligned. Alignment was necessary because the microscope drifted slightly during the time between the acquisition of successive images. The procedure first detected the walls of the microchannel using the Sobel Edge Operator, as shown in Fig. 4b. Next, the channel dimensions were approximated as a rectangle by fitting the Sobel-detected edges with the best-fit horizontal and vertical lines, as shown in Fig. 4c. The height of the channel was measured to be  $h = 130 \pm 2 \mu\text{m}$  and the width of the channel was measured to be  $w = 128 \pm 2 \mu\text{m}$ . The uncertainty in measuring  $w$  arose from the fabrication process—the microchannel was not completely square; specifically, the microchannel was slightly wider at the top than the bottom. The uncertainty in measuring  $h$  was a

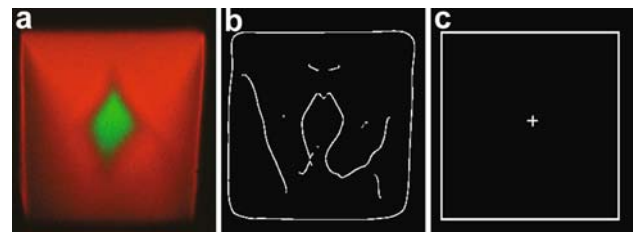


**Fig. 4** Image registration. **a** Confocal microscopy image prior to image processing. **b** Result of the Sobel edge-detection operator. **c** Rectangular approximation to the walls of the microchannel. The geometric center of the microchannel is shown with a plus symbol

consequence, in part, of the distance in depth between successive scan-lines of  $1 \mu\text{m}$ . The error associated with measuring the location of each wall of the microchannel was estimated by calculating the standard deviation of the Sobel-detected edge pixels about the line best-fit to the wall of the microchannel, as described in Sect. 3.4.

#### 4.3.2 Spectral unmixing

Cross-talk between the red and green channels of photo-detection was removed by a linear spectral unmixing procedure. This procedure corrected for the partial overlap in emission spectra of rhodamine and fluorescein, separating the two contributions from the acquired spectrum and allowing for the calculation of the contribution of each dye to each pixel's intensity. Our procedure and its effect on the images are described in Appendix.

#### 4.3.3 Depth-dependence compensation

The decay in the image brightness along the depth of the microchannel was corrected using a mathematical correction procedure. Our procedure and its effect on the images are described in Appendix.

#### 4.3.4 Measurement of the center-of-mass of the fluorescein-labeled fluids

The center of mass of fluorescein was calculated according to the usual formula as described in the Sect. 3.5. This calculation was performed on both the experimental images and the simulations, and an example of the result of these calculations is shown for the flow-rate condition  $U_3/U_2 = 11$  in Fig. 5. The center of mass of the experimental image was located at  $x_{\text{CM}} = 0.51 \pm 0.02$  and  $y_{\text{CM}}^{\text{EXP}} = 0.28 \pm 0.02$ , as shown in Fig. 5a, while the center of mass of the simulated image was located at  $x_{\text{CM}}^{\text{SIM}} = 0.50$  and  $y_{\text{CM}}^{\text{SIM}} = 0.27$ , as shown in Fig. 5b. The stated values of  $x_{\text{CM}}$  and  $y_{\text{CM}}$  are both normalized by the height,  $h$ , and width,  $w$ , of the microchannel as measured from the experimental images during the image registration procedure. The error

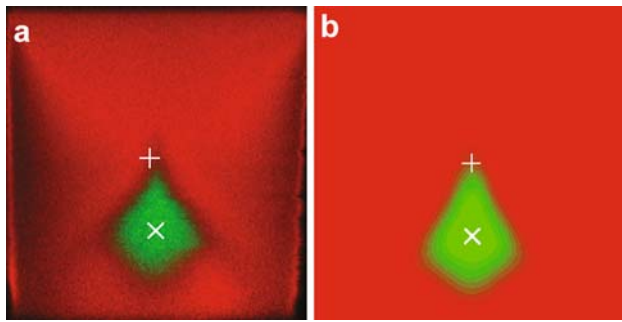


**Fig. 5** Fluorescence micrograph and simulation showing the center of mass of the fluorescein-labeled fluids. **a** Confocal microscopy image, **b** simulation. The geometric center of the microchannel is specified by *plus symbol* and the center of mass of the fluorescein-labeled fluids is specified by *multi symbol*

associated with the center-of-mass measurements was dominated by the error associated with measuring the position of the top and bottom walls of the microchannel (Sect. 3.4), and was therefore independent of  $U_3/U_2$ .

#### 4.4 Effect of the relative rates of the focusing fluids on the vertical position of the fluids-under-focusing

The experimental values of the center-of-mass of fluorescein,  $y_{CM}$ , are scatter-plotted against the ratio of the upper to lower focusing flow-rates,  $U_3/U_2$ , in Fig. 6, and the simulations are represented by a dashed curve on the same plot. The curve representing  $y_{CM}$  according to the simulations is antisymmetric about a point-of-inflection which occurs at  $U_3/U_2 = 1.5$ . This curve decreases monotonically, more steeply near the point of inflection and leveling

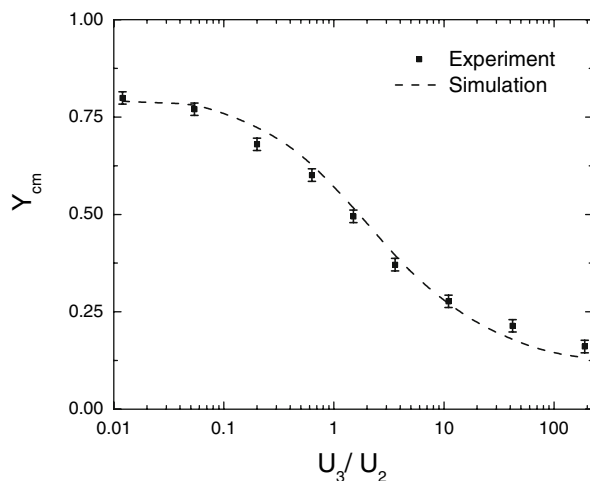


**Fig. 6** Effect of the ratio of the upper and lower focusing flow rates on the vertical position of the focused stream. The location of the center-of-mass of the fluorescein-labeled fluid is plotted against the ratio of the flow-rate of the upper focusing fluid to the flow-rate of lower focusing fluid,  $U_3/U_2$

off at extreme values of  $U_3/U_2$ ; the experimental data follow all of these trends, verifying the accuracy of our simulations. Notably, the manifold required a greater amount of focusing fluid at the upper (second) focusing input relative to the lower (first) focusing input in order to position the sample vertically at the geometric center of the microchannel; specifically,  $y_{CM}|_{U_3/U_2=1.5} = 0.52$  whereas  $y_{CM}|_{U_3/U_2=1.0} = 0.57$ , according to the simulations.

## 5 Conclusions

A simple microlithographic hydrodynamic focusing manifold was developed which vertically steers the focused sample in a predictable manner upon adjustment to the focusing flow-rates. The movement of the sample in response to adjustments to the flow-rates was imaged with confocal microscopy and simulated with commercially available multiphysics software. Based on a simple center-of-mass measurement, the simulations accurately predicted the position of the focused stream as the ratio of the upper to lower focusing flow-rates was swept over a range of four-orders of magnitude.

The manifold was fabricated by standard replica molding techniques and can be readily integrated into lab on-a-chip devices for applications. The design reduces the number of fluid inputs required to achieve three-dimensional focusing compared with previous designs (Chang et al. 2007), making this design particularly useful for the development of portable biosensors by reducing the number of required on-board fluid pumps. The manifold was designed with a feature height equal to the diameter of a standard optical fiber; therefore, using the dimensions and fabrication procedure presented in this paper, the manifold can be integrated into a microfabricated flow cytometer of the type containing imbedded optical fibers (Tung et al. 2004). In addition, the manifold and techniques described in this paper could be used to develop integrated opto-fluidic devices. For example, efficient coupling between solid-core waveguides and liquid-core/liquid-cladding waveguides (Wolfe et al. 2004) should be made possible by precise steering of the high refractive index core of the fluidic waveguide. For such applications, it should be possible to steer the focused stream in both the horizontal and vertical directions (see Nieuwenhuis et al. 2003) by adjusting, in addition to  $U_3/U_2$ , the relative rates of the focusing fluids from the left versus the right side of the manifold.

**Acknowledgments** This work was supported in part by the National Institute of Justice (NIJ #2004-DN-BX-K001) and the Ludwig Institute for Cancer Research. S.L.P. thanks the Intel Foundation and the National Nanotechnology Infrastructure Network Research Experience for Undergraduates (NNIN REU) Program. This work was

performed in part at the Cornell NanoScale Facility, a member of the National Nanotechnology Infrastructure Network, which is supported by the National Science Foundation. Images were acquired at the Microscopy and Imaging Facility of the Cornell University Life Sciences Core Laboratories Center. M.J.K. thanks Anthony Reeves for discussions about the image processing and Carol Bayols for advice on the two-color imaging experiment.

## Appendix: Image processing

The experimental images were modified using two image processing procedures: spectral unmixing and depth-dependence compensation. An implementation of these procedures was written in MATLAB, and a detailed description is provided here for the interested reader.

The net effect of image processing is shown in Fig. 7. The spectral bleedthrough of rhodamine into the green-channel is present in the original image shown in Fig. 7a, but after image processing, the rhodamine appears purely red because the bleedthrough effect has been subtracted out of the processed image shown in Fig. 7b. Also, the original image is brighter near the top of the microchannel than

near the bottom, but the brightness of the processed image is more uniform with depth because the image has been compensated for the depth-dependent response of the optical experiment.

## Spectral unmixing

A flat-field image was acquired in which all inputs to the flow-cell contained rhodamine. Ideally, the rhodamine would be detected as purely red and the pixel green-values of this image would be zero everywhere. However, rhodamine was detected not only by the red-channel photodetector but also by the green-channel photodetector, and therefore the pixel green-values were non-zero and were observed to be directly proportional to the red-values. Moreover, the fraction of the red bleeding into the green depended on depth. The factor of spectral bleedthrough along the depth of the channel,  $F_S(y)$ , was obtained by averaging the pixels horizontally and then dividing the average green-value of each row of pixels by the average red-value of each row of pixels. It was found that  $F_S(y)$  was equal to 17% near the top of the channel and 10% near the bottom of the channel.

The effect of spectral bleedthrough was removed from each experimental image by subtracting the appropriate quantity from the pixel green-values according to the following formula, where  $I_G$  and  $I_R$  represent the pixel green-values and red-values of the original image and  $\tilde{I}_G$  represents the pixel green-values of the unmixed image:

$$\tilde{I}_G(x, y) = I_G(x, y) - F_S(y) \cdot I_R(x, y).$$

Prior to the subtraction procedure, the pixel green-values near the top of the microchannel were brighter than background, as shown in Fig. 7c, but after the subtraction procedure, the pixel green-values were bright only in the region of the fluorescein-containing fluids, as shown in Fig. 7d. This straightforward subtraction technique provides a computationally simple implementation of linear unmixing and is possible in our case because only rhodamine was detected in both the red and the green whereas fluorescein was detected only by the green-channel photodetector (Zimmermann 2005).

## Depth-dependence compensation

Depth-dependence compensation was required because the original images were bright near the top of the microchannel and dim near the bottom of the microchannel. This depth-dependence of image brightness did not reflect the concentration distributions of the fluids but resulted from uneven illumination along the depth of the specimen and imperfections of the optical detection system of the microscope.

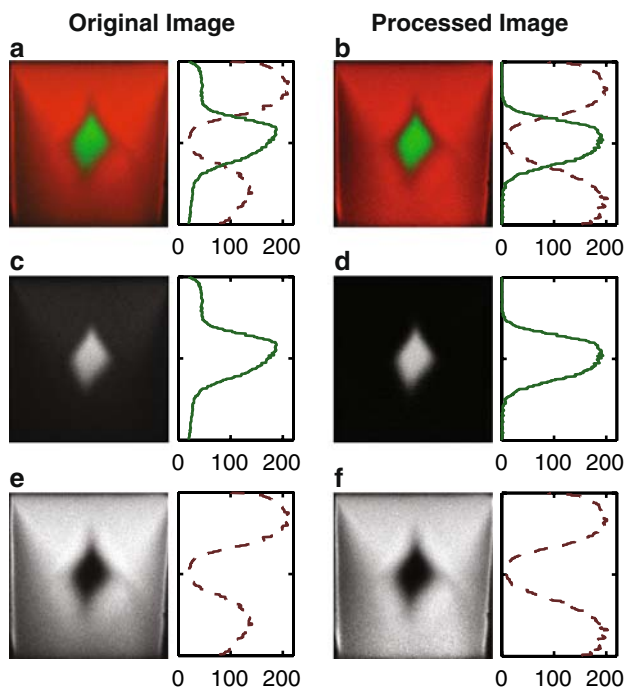


**Fig. 7** Fluorescence micrographs and intensity profiles showing the effect of image processing. **a** Original image alongside a profile of the pixel green-values (solid line) and pixel red-values (dashed line) obtained along the vertical center of the image. The image pixels contained integer values between 0 and 255. In each of the pixel profiles,  $y$  varies along the vertical axis from  $y = 0$  to  $y = 1$ . **b** Processed image; **c** original image, pixel green-values; **d** processed image, pixel green-values; **e** original image, pixel red-values; **f** processed image, pixel red-values



The spatial decay of light intensity with depth has been encountered previously in three-dimensional confocal microscopy, and two competing methods have been used to correct this decay: image arithmetic and mathematical correction. The image arithmetic approach normalizes the images according to a formula originally developed for fluorescence microscopy (Park et al. 2004):

$$CI = \frac{OI - DF}{FF - DF},$$

where OI represents the original image, CI represents the corrected image, DF represents the dark-field image in which no dye is present, and FF represents the flat-field image in which dye is uniformly present. This technique relies heavily on the precise alignment of the dark-field image to the flat-field and experimental images. In practice, however, it can be difficult to register the dark-field image to the experimental images because the walls of the microchannel cannot be detected in the absence of fluorescently stained fluids. For this reason, we elected to restore the images using a mathematical correction method.

Several alternative mathematical correction methods have been developed to correct confocal microscopy images suffering from the effect of depth-decay of brightness (Umesh and Chaudhuri 2000). Seeking ease of computation, we have developed a simple method of correction based on a linear fit and linear transformation. Our procedure begins by describing the decay of image brightness with depth based on the flat-field images. Two flat-field images were obtained: first, all of the fluid inputs to the flow-cell were loaded with rhodamine and a red flat-field image was acquired,  $I_R^{FF}$ ; second, all of the fluid inputs were loaded with fluorescein and a green flat-field image was acquired,  $I_G^{FF}$ . A horizontal median filter was applied to the flat-field image in which fluorescein-labeled fluid was pumped into all of the inputs of the flow-cell by using the *nlfilter()* function of MATLAB with a sliding block of  $20 \times 1$  pixels. Then, a profile was obtained vertically up the center, revealing a profile of the depth-dependence of the intensity of fluorescence,  $I_G^{FF}(y)$ . The parameters describing the depth-dependence were obtained by fitting this profile with the following equation:

$$I_G^{FF}(y_C - y)|_{y < y_C} = m_G \cdot (y_C - y) + b_G$$

$$I_G^{FF}(y_C)|_{y > y_C} = b_G$$

where a characteristic height was identified,  $y_C$ , above which the image brightness was approximately constant and below which the brightness decayed approximately linearly, and where the fitting parameters  $m_G$  and  $b_G$  were obtained by linear regression. For the green flat-field image,  $I_G^{FF}(x, y)$ , this decay occurred for  $y < y_G^C$ , where  $y_G^C = 0.63$  and  $y$  is measured from the bottom of the microchannel and is normalized between zero and one. The slope of decay was

$m_R = -1.9 \pm 0.1 \mu\text{m}^{-1}$ , and the intercept at  $y_G$  was  $b_G = 217 \pm 3$ ; here, it is useful to recall that the pixel-values of the original image were 8-bit integers ranging from 0 to 255. The fitting procedure was repeated similarly for the red flat-field image,  $I_R^{FF}(x, y)$ , and it was found in this case that  $y_R^C = 0.49$ ,  $m_R = -1.9 \pm 0.1 \mu\text{m}^{-1}$ , and  $b_R = 213 \pm 9$ . Restated, the brightness of the green flat-field image decayed from  $I_G^{FF} \approx 217$  at a critical depth of  $48 \mu\text{m}$  to  $I_G^{FF} \approx 61$  near the bottom of the microchannel, with a constant rate of decay of  $1.9 \mu\text{m}^{-1}$  at depths beyond than the critical depth. Similarly, the intensity of the red flat-field image decayed from  $I_R^{FF} \approx 213$  at a critical depth of  $66 \mu\text{m}$  to  $I_R^{FF} \approx 91$  near the bottom of the microchannel, with a constant rate of decay of  $1.9 \mu\text{m}^{-1}$ . In the top portion of the image, above the critical depth, the brightness in each of the flat-field images was approximately constant.

With these parameters at hand, each experimental image was restored of depth decay by applying the following transformation independently to the red color-component of the image,  $I_R(x, y)$ , and the green color-component of the image,  $I_G(x, y)$ , where  $I'(x, y)$  is the corrected image:

$$I'(x, y) = I(x, y) \cdot \frac{b}{m \cdot y + b}.$$

Prior to the procedure, the pixel red-values were less bright near the bottom of the microchannel than near the top of the microchannel, as shown in Fig. 7e, but after the procedure, the pixel red-values near the top and bottom of the microchannel were of similar brightness, as shown in Fig. 7f.

## References

- Chang C-C, Huang Z-X, Yang R-J (2007) Three-dimensional hydrodynamic focusing in two-layer polydimethylsiloxane microchannels. *J Micromech Microeng* 17(8):1479–1486
- Dickinson ME et al (2001) Multi-spectral imaging and linear unmixing add a whole new dimension to laser scanning fluorescence microscopy. *Biotechniques* 31(6):1272–1279
- Fu L-M, Yang R-J, Lin C-H, Pan Y-J, Lee G-B (2004) Electrokinetically driven micro flow cytometers with integrated fiber optics for on-line cell/particle detection. *Anal Chim Acta* 507:163–169
- Goddard GR et al (2007) Analytical performance of an ultrasonic particle focusing flow cytometer. *Anal Chem* 79(22):8740–8746
- Holmes D, Morgan H, Green NG (2006) High throughput particle analysis: combining dielectrophoretic particle focussing with confocal optical detection. *Biosens Bioelectron* 21(8):1621–1630. doi:10.1016/j.bios.2005.10.017
- Knight JB et al (1998) Hydrodynamic focusing on a silicon chip: mixing nanoliters in microseconds. *Phys Rev Lett* 80(17):3863. doi:10.1103/PhysRevLett.80.3863
- Kohlheyer D et al (2008) A microfluidic device for array patterning by perpendicular electrokinetic focusing. *Microfluid Nanofluid* 4(6):557–564. doi:10.1007/s10404-007-0217-9

- Laulicht B et al (2008) Evaluation of continuous flow nanosphere formation by controlled microfluidic transport. *Langmuir* 24(17):9717–9726
- Mao X, Waldeisen JR, Huang TJ (2007) “Microfluidic Drifting”-implementing three-dimensional hydrodynamic focusing with a single-layer planar microfluidic device. *Lab Chip* 7:1260–1262
- McClain MA et al (2001) Flow cytometry of *Escherichia coli* on microfluidic devices. *Anal Chem* 73(21):5334–5338
- Nieuwenhuis JH et al (2003) Integrated flow-cells for novel adjustable sheath flows. *Lab Chip* 3:56–61
- Park SJ et al (2004) Rapid three dimensional passive rotation micromixer using the breakup process. *J Micromech Microeng* 14:6–14
- Pollack L et al (2001) Time resolved collapse of a folding protein observed with small angle X-ray scattering. *Phys Rev Lett* 86(21):4962. doi:[10.1103/PhysRevLett.86.4962](https://doi.org/10.1103/PhysRevLett.86.4962)
- Shin S-J et al (2007) “On the fly” continuous generation of alginate fibers using a microfluidic device. *Langmuir* 23(17):9104–9108
- Simonnet C, Groisman A (2005) Two-dimensional hydrodynamic focusing in a simple microfluidic device. *Appl Phys Lett* 87(11):114104
- Sundararajan N et al (2004) Three-dimensional hydrodynamic focusing in polydimethylsiloxane microchannels. *J Microelectromech Syst* 13(4):559–567. doi:[10.1109/JMEMS.2004.832196](https://doi.org/10.1109/JMEMS.2004.832196)
- Tung Y-C et al (2004) PDMS-based opto-fluidic micro flow cytometer with two-color multi-angle fluorescence detection capability using PIN photodiodes. *Sens Actuators B* 98:356–367
- Umesh APS, Chaudhuri BB (2000) Some efficient methods to correct confocal images for easy interpretation. *Micron* 32(4):363–370
- Wang Z et al (2004) Measurements of scattered light on a microchip flow cytometer with integrated polymer based optical elements. *Lab Chip* 4:372–377
- Wolfe DB et al (2004) Dynamic control of liquid-core/liquid-cladding optical waveguides. *Proc Natl Acad Sci* 101(34):12434–12438
- Zhao Y et al (2007) Optical gradient flow focusing. *Opt Express* 15(10):6167–6176
- Zimmermann T (2005) Spectral imaging and linear unmixing in light microscopy. *Adv Biochem Eng Biotechnol* 95:245–265